Journal of Applied Physics ARTICLE pubs.aip.org/aip/jap

Structure of $Zn_xFe_{3-x}O_4$ nanoparticles studied by neutron diffraction and its relation with their response in magnetic hyperthermia experiments

Cite as: J. Appl. Phys. **136**, 043905 (2024); doi: 10.1063/5.0214250
Submitted: 16 April 2024 · Accepted: 6 July 2024 ·
Published Online: 23 July 2024

J. Lohr,[1,2] D. Tobia,[3,a)] T. E. Torres,[4,b)] L. Rodríguez,[3] I. Puente Orench,[4,5] G. J. Cuello,[5] M. H. Aguirre,[4] J. Campo,[4] G. Aurelio,[1,2] and E. Lima, Jr.[3]

AFFILIATIONS

[1]Comisión Nacional de Energía Atómica–Laboratorio Argentino de Haces de Neutrones, Centro Atómico Bariloche, Av. Bustillo 9500 R8402AGP, S. C. de Bariloche, Argentina
[2]Consejo Nacional de Investigaciones Científicas y Técnicas (CONICET), S. C. de Bariloche, Argentina
[3]Instituto de Nanociencia y Nanotecnología CNEA-CONICET, Centro Atómico Bariloche, S. C. de Bariloche, 8400, Argentina
[4]Instituto de Nanociencia y Materiales de Aragón, Universidad de Zaragoza- CSIC, C/Pedro Cerbuna 12, E-50009 Zaragoza, Spain
[5]Institut Laue Langevin. 71, Av des Martyrs, BP 156, F-38042, Grenoble, France

[a)]**Author to whom correspondence should be addressed:** dina.tobia@cab.cnea.gov.ar
[b)]**Previous address:** Instituto de Nanociencia y Nanotecnología CNEA-CONICET, S. C. Bariloche, 8400 Argentina.

ABSTRACT

The mixed zinc-ferrite spinel magnetic nanoparticles (MNPs) with the general formula $Zn_xFe_{3-x}O_4$ are among the most extensively studied families of Fe oxides due to their interesting and diverse chemical, electronic, and magnetic properties. These systems offer the possibility of surface functionalization and possess high biocompatibility, making them highly attractive for applications in biomedicine, such as magnetic fluid hyperthermia (MFH). The efficiency of the MFH process relies on the magnetic, structural and morphological properties of the MNPs. The substitution with the Zn ion and the cationic distribution, as well as the synthesis process employed, have a direct impact on the final properties of these oxides. Therefore, it is essential to have tools that enable a comprehensive characterization of the system to assess its performance in MFH. In this study, we have synthesized four $Zn_xFe_{3-x}O_4$ MNP systems using three different methods: two by thermal decomposition at high temperatures, one by co-precipitation, and another by co-precipitation followed by ball milling. We analyze the effect of these various synthesis processes on the magnetic and crystallographic properties, aiming to correlate them with the response of each system in MFH. Neutron diffraction data are employed to determine the cation site occupation and to investigate the correlation with the synthesis method. MFH measurements were conducted in media of diverse viscosities, revealing different values of specific loss power, thus demonstrating a clear dependence on the synthesis process and Zn content.

INTRODUCTION

One primary objective in the preparation of nanoparticles (NPs) is to be able to control and tune their properties at an atomic level in the closest way. The attainment of these goals enables the modulation of various responses of the NPs tailored for specific or multiple functions. This objective has led to the development of several chemical preparation methods, commonly referred as bottom-up approaches. In these approaches, the nanoparticulate material is constructed from small clusters, molecules, or directly from individual atoms.[1–3]

The crystalline structure in a nanomaterial plays a crucial role in fine-tuning its properties and enabling multifunctional capabilities. The connection of the crystal structure with the properties of magnetic nanoparticles (MNPs) is particularly strong, exerting a significant influence on factors such as magnetic order, magnetization, susceptibility, anisotropy, and magnetic moment relaxation

mechanisms.[4–7] A possible application of MNPs consists in tuning such relaxation mechanism and time, thus controlling their response to external magnetic fields, especially *ac* ones.[8,9]

Among the experiments involving MNPs with attractive potential applications, magnetic fluid hyperthermia (MFH) holds significant interest in medical processes, where a target tissue is attacked by or permeated because of heating,[10] as well as in chemical processes such as catalysis[11] or in an accelerated or controlled polymerization process.[12] In MFH, energy is absorbed from an *ac* magnetic field applied by a system of MNPs dispersed in a medium. This absorption occurs due to the dephasing between the applied *ac* field and the magnetic moment. This is followed by heat generation and an increment of temperature in the vicinity of the MNPs. Thus, one of the key parameters for the effective performance of a nanoparticle system in MFH is the magnetic relaxation time. This parameter is strongly dependent on the morphology, crystallinity, and magnetic properties of the MNPs, both individually and as an ensemble attributed to interparticle magnetic interactions. A better control of these characteristics is achieved by adjusting the synthesis method and the thermal history of the sample to obtain the desired morphology and crystallinity of the MNP system.

Major scientific and technological efforts have been devoted to the study of MFH experiments with *ac* magnetic fields with varying amplitudes and frequencies. This includes noteworthy multinational projects aimed at parameterizing and standardizing the response of MNPs prepared through diverse procedures, exhibiting different sizes, compositions, morphologies, crystallinity, and magnetic properties. However, this enterprise is far from complete and many detailed studies are still needed. In the MFH experiments, the magnetic relaxation dynamics is typically modeled by two mechanisms, viz., the Brown or mechanical relaxation, characterized by a relaxation time τ_B, and the Néel, or magnetic relaxation, with a characteristic time τ_N. The Brownian relaxation depends on the rheological properties of the system, such as the viscosity of the medium (η) and hydrodynamic volume (V_{hyd}) of the MNPs. Likewise, τ_N is associated with the fluctuation of the magnetic moment through the anisotropy energy barrier $K_{eff}V$, where K_{eff} is the effective anisotropy constant and V is the volume of the particle. Typically, both mechanisms occur simultaneously, with the predominant relaxation process determined by the shorter relaxation time. Optimizing the magnetic properties of the particles according to the medium of action enables a more efficient response in magnetic losses.

Research on MFH based on MNPs is predominantly centered on ferrite systems with the general chemical formula $M_xFe_{3-x}O_4$ (where M is a cation). This focus stems from their high chemical and structural stability coupled with magnetic properties that can be finely tuned by the incorporation and site distribution of different cations in the spinel structure.[13,14] Specifically, the $Zn_xFe_{3-x}O_4$ ferrites are known for their good performance in MFH.[15] Their magnetic properties exhibit a strong dependence on *x*, the amount of Zn substitution, influencing magnetocrystalline anisotropy (which varies from 1 to 10×10^4 erg/cm^3) and saturation magnetization M_S (reaching up to 98 emu/g in a ferrimagnetic state).[15,16] In this compound, the magnetic response and the performance in MFH depend directly on the Zn amount and on the distribution of Zn and Fe atoms in the interstitial A-site (with tetrahedral oxygen coordination) or the B-site (with octahedral oxygen coordination) of the spinel structure. Despite that, the Zn^{2+} atomic diameter would suggest a preferential incorporation of Zn in the A-site,[17] and it has been shown that the cationic distribution between A and B sites actually depends on the crystallinity of the material and on the synthesis method. This phenomenon, known as the inversion degree, leads to drastic changes in the magnetic order and magnetic properties of the Zn-ferrite NPs.[18–21] Furthermore, the equilibrium magnetic structure of the $x = 1$ ferrite, $ZnFe_2O_4$, remains a subject of research despite several decades of investigation, even for the bulk compound. Long-range antiferromagnetic (AFM) order has been observed below 10 K [with a propagation vector $\boldsymbol{k} = (1\ 0\ ½)$],[22,23] along with claimed short-range AFM order. However, particles prepared through non-equilibrium methods exhibit a transition to ferrimagnetic (FiM) or ferromagnetic (FM) ordering at significantly higher temperatures: around 30 K for coprecipitation methods[24] and above 77 K for ball-milled NPs.[25] This is attributed to the fact that an increase in the inversion parameter results in the redistribution of Fe^{3+}, Fe^{2+}, and oxygen vacancies, favoring super-exchange interactions. Not only does the inversion degree influence the magnetic order, but particle size may also play a role. This was explored by Hofmann *et al.*[26] and Ehrhardt *et al.*,[27] who found that coarse-grained samples present AFM long-range order that is gradually destabilized by milling, shifting to short-range AFM order, and finally to a FiM order with further grinding, i.e., size reduction. Over this complex scenario, the effect of gradually replacing Zn with Fe, which turns the spinel from normal to inverse, is still to be considered.

Neutron beam-based techniques, particularly diffraction and small-angle scattering, are powerful tools for investigating nanomaterials, providing detailed insights into their morphology, crystal structure, and magnetic order.[28–30] The difference in the coherent neutron scattering lengths between Zn and Fe ($b_{Zn} = 5.68$ vs $b_{Fe} = 9.45$ fm) is advantageous for the correct determination of cation occupancy in diffraction experiments. Consequently, neutron data are anticipated to yield better contrast, ensuring a more reliable determination of the inversion parameter. Moreover, in x-ray scattering experiments, the precise determination of oxygen positions is impeded by the strong scattering of Zn and Fe. In contrast, neutron scattering benefits from the comparable oxygen scattering length ($b_O = 5.803$ fm). Thus, neutron powder diffraction (NPD) proves to be better suitable than x-ray diffraction (XRD) for precisely determining the positions of oxygen atoms. Finally, the interaction between the neutron magnetic moment and the internal fields provides valuable information about the magnetic order of the NPs.

The interplay of particle size, preparation method, and effective Zn^{2+} content is important to determine the kind of magnetic order exhibited by MNPs under various conditions. NPD emerges as a highly valuable tool for elucidating these phenomena. The magnetic properties, as determined by compositional and morphological characterizations, delineate the suitability of MNPs for specific applications based on the magnetic response, such as in MFH. The integration of NPD with complementary techniques like transmission electron microscopy (TEM), and elemental spectroscopic techniques, such as particle-induced x-ray emission (PIXE) or energy-dispersive x-ray spectroscopy (EDS), facilitates a very detailed description of the structural and magnetic properties

of distinct NPs obtained through different routes, with variable composition and synthesis methodologies. Such a comprehensive understanding is necessary to shed some light on the correlations among synthesis method, crystal structure/morphology, and magnetic properties.

In this work, $Zn_xFe_{3-x}O_4$ MNPs were synthesized with varying diameters, size dispersion, and Zn content (x) through two bottom-up chemical methods: modified-polyol (thermal decomposition) and coprecipitation, as well as one physical top-down method: high-energy ball milling. The synthesized MNPs underwent comprehensive characterization by XRD, NPD, TEM-EDS, PIXE, and macroscopic magnetic measurements. This multi-technique approach aimed to establish correlations between morphological, compositional, and crystallographic properties with the magnetic response and the performance of each system in MFH experiments.

EXPERIMENTAL

$Zn_xFe_{3-x}O_4$ nanoparticle preparation

Four samples were synthesized for the present study: two samples were produced using the thermal decomposition method (TD1 and TD2), one using the coprecipitation method (CP) and one through high-energy ball milling of the annealed coprecipitated MNPs (BM).

For the samples prepared through the thermal decomposition method, the reaction of iron (III) and Zn (II) acetylacetonates (acac) was done with 1,2- octanediol (diol), using benzyl ether as a solvent in the presence of oleic acid (OA) and oleylamine (OLA) as surfactants. Molar ratios of 1:3:1:0.5 between the precursor, surfactants (OA and OLA), and diol were employed to control the final particle size. Different ratios between Fe and Zn acetylacetonates were mixed for TD1 and TD2, in particular (19.7 and 16.4) mmol of $Fe(acac)_3$, (1.1 and 4.4) mmol of $Zn(acac)_2$ were, respectively, mixed with 62.4 mmol of OA, 20.8 mmol OLA, 10.4 mmol of 1,2 octanediol, and 280 ml of benzyl ether and mechanically stirred under a flow of nitrogen. The mixture was heated to 200 °C for 60 min and then heated to reflux (298 °C) for another 90 min. The resulting mixture was cooled to room temperature by removing the heat source. Under ambient conditions, ethanol and acetone were added to the mixture. A black material precipitated, which was separated magnetically. The final product was dispersed and kept in hexane.

Sample CP was prepared by slowly dropping 10 ml of an aqueous solution containing 1.49 g of $FeCl_2{\cdot}4H_2O$ (7.5 mmol) and 4.31 g (15 mmol) of $FeCl_3.7H_2O$ at a rate of 1 drop/s in 70 ml of a NaOH solution with pH = 11 at 60 °C, under N_2 flux and strong mechanical stirring. Throughout the dropping procedure, lasting approximately 10 min, the pH was monitored. Upon observing a decrease in pH to the value of 8, it was adjusted back to pH 11 by adding more NaOH to the solution. After the dropping procedure, the solution was maintained at 60 °C for 1 h and then cooled down. The resulting nanoparticles were magnetically precipitated, washed once with milli-Q water and twice with ethanol. Subsequently, the precipitated powder was air-dried overnight at 110 °C and then annealed in atmospheric air at 250 °C for 2 h.

For sample BM, a portion of the as-prepared CP nanoparticles was isolated and manually ground in an agate mortar. Subsequently, this powder was ball-milled in a Spex Ball Mill 8000 at a maximum power for 40 min using a vial and stainless steel spheres. The mass ratio of balls to sample used was 10:1.

Characterization methods

The composition of the as-prepared nanoparticles was determined by PIXE[31] with a 3 MeV H^+ beam obtained from a NEC 5SDH 1.7 MV tandem accelerator and a NEC RC43 end-station. The MNPs produced by thermal decomposition underwent multiple washes with acetone to reduce the remaining amounts of oleic acid and oleylamine from the synthesis. The other samples were used directly after drying (sample CP) or from the vial (sample BM). All powders for PIXE measurements were conditioned by placing them over a carbon tape, and the results were analyzed using the software GUPIX.[32]

TEM images were obtained in a TECNAI F20 microscope operating at 200 kV and equipped with an EDS (energy-dispersive x-ray spectroscopy) detector. For the TD samples, TEM specimens were prepared by dropping a solution of MNPs dispersed in toluene onto a copper grid coated with an amorphous carbon layer. Samples CP and BM were dispersed in isopropanol. EDS analyses were conducted in selected regions to provide additional compositional information.

For the initial characterization, XRD patterns of all samples were collected at room temperature in a Panalytical Empyrean diffractometer using Cu-K_α radiation (1.5406 Å) in a Bragg–Brentano geometry. The measurements were conducted between 10° and 90° with a step size of 0.02°, using a low-background sample holder.

The NPD experiments were performed at the Institut Laue Langevin in Grenoble (France), utilizing the D1B diffractometer with two different wavelengths, $\lambda = 2.52$ Å for the optimal flux and $\lambda = 1.28$ Å for enhanced resolution.[33] Powder samples TD1, TD2, CP, and BM were placed in 5 mm-diameter vanadium cans mounted onto a cryo-furnace. Full diffraction patterns were collected with an average acquisition time of 30 min at selected temperatures. The obtained XRD and NPD patterns were analyzed using the FullProf suite.[34,35] Precise wavelength values were calibrated from standard samples measurements of Si and $Na_2Ca_3Al_2F_{14}$ powders, yielding the values $\lambda_1 = 1.2876 \pm 0.0001$ Å and $\lambda_2 = 2.5268 \pm 0.0001$ Å. The background was modeled with a 9-term Chebychev polynomial. Rietveld refinements were performed using the structure for zinc ferrite after Solano *et al.*[36] as a starting point, corresponding to the *Fd-3m* space group (origin choice 2). In this structure, oxygen anions occupy 32e Wyckoff positions (¼ + u, ¼ + u, ¼ + u), whereas the Fe and Zn cations are distributed into the octahedral 16d (½, ½, ½) and tetrahedral 8a (⅛, ⅛, ⅛) positions according to a model based on the inversion degree δ. The refined parameters included the lattice parameter (a), scale factor, fractional coordinate of the oxygen atom (u), background coefficients, 2-theta offset, and the isotropic temperature factors for all atoms. The inversion degree δ was modeled to keep the sample's neutrality and preserve the average Zn content obtained experimentally from PIXE measurements.

The peak profiles were modeled using the Thompson-Cox-Hastings formulation of the pseudo-Voigt function. The instrumental contribution to the total peak broadening was determined by refining data from a $Na_2Ca_3Al_2F_{14}$ standard, measured under

the same conditions as the samples. The obtained instrumental resolution function was then used to deconvolute the sample contribution to broadening. A Lorentzian peak shape parameter, Y, related to isotropic size broadening, was refined, assuming spherical strain-free crystallites. The crystallite sizes were calculated using the Scherrer formula, $\langle D\rangle = (K \cdot \lambda)/[\beta\cos(\theta)]$, where $\langle D\rangle$ is the mean volume-weighted size of the coherently scattering crystalline domains, λ is the wavelength, θ is the scattering angle, β describes the peak broadening, and K is the shape factor, assuming isotropic crystallite morphology.

The magnetization of the samples as a function of the applied field was measured at room temperature in a vibrating sample magnetometer (VSM, Lakeshore) and at 5 K in a commercial superconducting quantum interference device magnetometer (SQUID, MPMS Quantum Design). Samples were conditioned by dispersing a known amount of material in a determined mass of a nonmagnetic epoxy resin, keeping the concentration below 0.5 wt. % This procedure avoids the physical rotation of the particles during the measurements and reduces the effects of dipolar interactions. In order to accurately determine the saturation magnetization M_S in the case of the TD samples, the amount of organic material was previously determined by thermogravimetric analysis and subsequently subtracted from the total mass for the magnetization measurements.

MFH experiments were performed in a F1-D5 RF commercial apparatus from nB Nanoscale Biomagnetics, Spain, operating with a magnetic field amplitude (H_0) of 200 Oe and a frequency of 571 kHz. In these experiments, the liquid solutions containing the samples were conditioned in a vacuum tube in order to reduce the heat losses. The measurements started at room temperature, and the temperature increment was measured with an optical thermometer. Distinct solvents with different viscosities (η) were employed to investigate the main relaxation mechanisms involved in each case. For the TD samples, which are hydrophobic, the first measuring solution consisted of 0.5 wt. % nanoparticles dispersed in oleic acid [η(293 K) = 35 mPa s],[37] while the second one consisted of 0.5 wt. % nanoparticles dispersed in hexane [η(295 K) = 0.3 mPa s].[38] For the CP and BM samples, 0.5 wt. % nanoparticles were dispersed in triethylene glycol [TEG—η(293 K) = 48 mPa s][39] or in ethanol [η(293 K) = 1.18 mPa s].[40]

RESULTS

The Zn content for each studied sample as obtained by PIXE is shown in Table I. It is notable that in the case of MNPs fabricated by thermal decomposition, Zn incorporated into the samples is much lower than expected from the stoichiometry of the starting precursors. This has been also observed in similar samples synthesized by the same route and can be associated with the limitation of Zn incorporation in the initial stage of the process when a strong reduction of Fe occurs, leading to the formation of a wüstite phase (FeO).[41,42] On the contrary, the Zn incorporation is more effective in the sample fabricated by the coprecipitation method.

Figure 1 shows representative TEM images of the synthesized samples: (a) and (b) correspond to those prepared by the thermal decomposition method, while (c) and (d) correspond to the sample prepared by coprecipitation and coprecipitation followed by ball milling, respectively. Noticeable differences in the morphology of the samples obtained by the different synthesis routes are clearly observed. The diameter histograms were constructed by measuring around 250 particles for each sample. Histograms were fitted with a lognormal distribution, yielding average diameters of 62 and 68 nm for samples TD1 and TD2, respectively, and 11 and 13 nm for samples CP and BM. Both samples synthesized by thermal decomposition present a similar size and size distribution; they exhibit faceted faces and low agglomeration due to the presence of remaining organic material on their surface. Conversely, samples CP and BM present a significantly smaller average size with respect to TD1 and TD2; they do not exhibit well-defined faces and show a greater degree of agglomeration.

Neutron diffraction

Room temperature NPD patterns were refined simultaneously for λ_1 and λ_2. To investigate the inversion degree and site preference of Zn^{2+}, PIXE results were used to constraint the total Zn composition. It is well-established that the $x = 1$ compound, $ZnFe_2O_4$, primarily exhibits a normal spinel structure, meaning Zn^{2+} tends to occupy solely the tetrahedral 8a sites. However, it has been noted that the compound can be prepared with $\delta \neq 0$. Non-equilibrium methods such as coprecipitation and ball milling may induce some degree of inversion impacting the magnetic properties of the zinc ferrite.[43,44] This mixed cation distribution is favored in nanosized zinc ferrites.

The refinements incorporated a linear restraint to fix the Fe/Zn ratio obtained by PIXE. These refinements resulted in negative values for the Zn occupation at the octahedral site, indicating that Zn^{2+} is exclusively located at the tetrahedral site 8a for all samples.

In agreement with observations in the TEM images, strong differences in the width of the diffraction peaks are evident in the

TABLE I. Compositional, morphological, and magnetic parameters for the different $Zn_xFe_{3-x}O_4$ MNPs. The Zn content x was determined by PIXE, SLP is the Specific Loss Power, M_S is the saturation magnetization at $T = 5$ K, D_{NPD} and $\langle D\rangle_{TEM}$ are the diameters of the NPs obtained from NPD and TEM analyses, respectively. The standard errors are given in parentheses, which refer to the last digit.

Sample	x (PIXE)	M_s @ 5 K (emu/g)	M_s @ 5K (μ_B/f.u.)	D_{NPD} (nm)	$\langle D\rangle_{TEM}$ (nm)	SLP (W/g_{MNP})	SLP (low viscosity media) (W/g_{MNP})
TD1	0.03 (1)	98.1 (1)	4.07	31 (1)	62 (13)	11 (1)	5 (1)
TD2	0.09 (1)	95.8 (1)	3.98	33 (1)	68 (14)	68 (1)	…
CP	0.39 (1)	85.0 (1)	3.58	8 (1)	11 (2)	19 (1)	10 (1)
BM	0.40 (1)	64.0 (1)	2.70	6 (1)	13 (3)	11 (1)	8 (1)

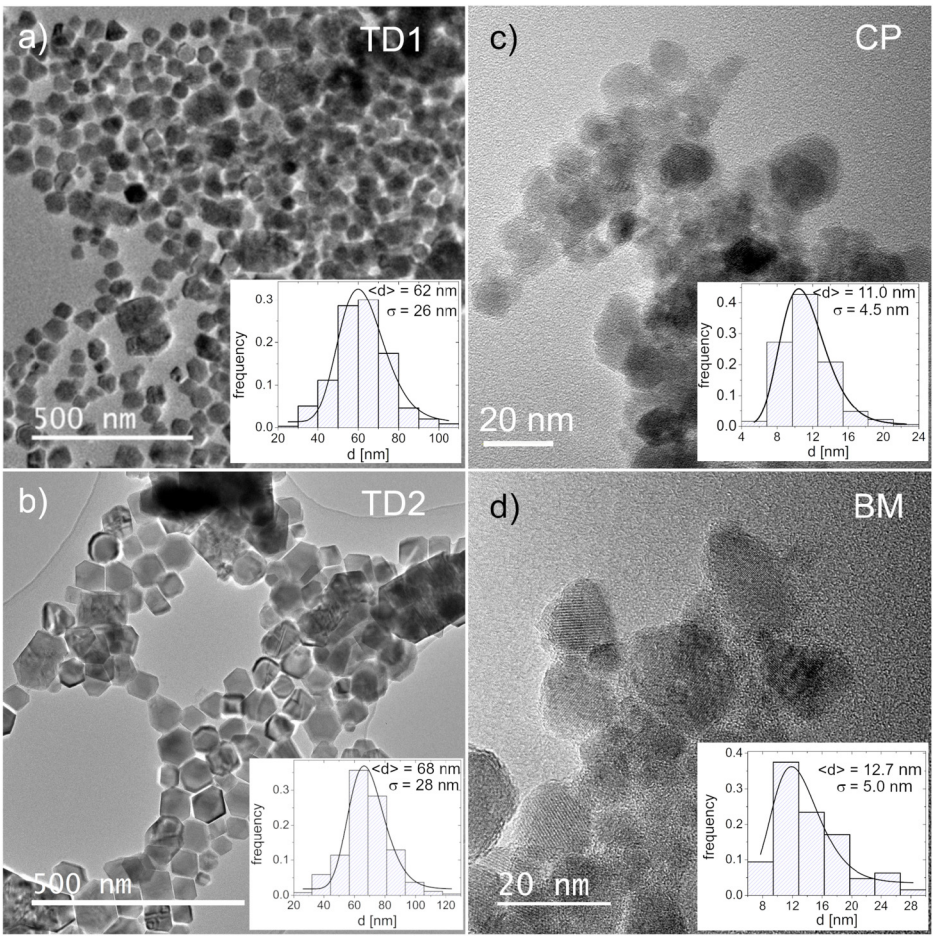

FIG. 1. Representative TEM images of the studied samples. (a) and (b) samples synthesized by thermal decomposition. (c) Sample synthesized by coprecipitation and (d) sample synthesized by coprecipitation followed by ball milling. The inset on each image shows the respective nanoparticle's diameter histogram fitted with a lognormal distribution along with the obtained values for the mean diameter ⟨d⟩ and dispersion σ.

diffractograms between the TD samples (TD1 and TD2) and samples BM and CP (Fig. 2). These differences can be linked to variations in their crystallize size as well as lattice strains and density of defect centers. To determine average size values, the instrumental contribution to peak broadening was eliminated, as outlined in the Experimental section. Crystallite diameters of 8(1), 6(1), 31(1), and 33(1) nm were obtained for CP, BM, TD1, and TD2, respectively, from the refinements of room temperature data, by using the Scherrer equation as implemented in FullProf.[34] This indicates that the average diameter of particle depends on the synthesis method, as expected. Although for all samples, the calculated diameter from NPD is about one half of the one observed by TEM, in the case of the CP and BM samples, this difference can be attributed to the observed agglomeration, which could mask the actual size of the individual nanoparticles. In the case of the TD samples, high-resolution TEM images revealed that many MNPs are actually conformed by two smaller grains (see Fig. S1 in the supplementary material). Moreover, TEM images represent a two-dimensional projection of the three-dimensional MNPs, potentially overlooking anisotropic morphologies through this technique.

In spinel structures with FiM or FM magnetic order, magnetic reflections in the diffractogram are observed along with the nuclear ones. The intensities of low-angle reflections cannot therefore be completely modeled by using only the nuclear phase, and the magnetic order needs to be included in the refinement. The results from NPD and magnetization measurements indicate that all the $Zn_xFe_{3-x}O_4$ MNPs measured in this work are magnetically ordered at room temperature, also confirmed by the magnetization measurements (Fig. 4). The data were successfully refined using the ferrimagnetic model based on the Fe_3O_4 spinel structure, corresponding to a collinear model with antiparallel moments on the tetrahedral and octahedral sites. The cartesian components of the magnetic moment were refined for the tetrahedral, μ_T, and octahedral sites, μ_o, respectively. The moments were constrained to align along ⟨111⟩, as expected in cubic lattices for materials with negative anisotropy (soft magnets), such as in the case of Zn ferrites.[45] A model of inverse spinel was employed, with one-half of the octahedral moments μ_{oa} constrained to be opposite and to have the same absolute value than the tetrahedral one, μ_T. The remaining magnetic moments were fixed along the ⟨111⟩ direction and refined. The left inset of Fig. 3 depicts the proposed model. The refined magnetic moments at the lowest

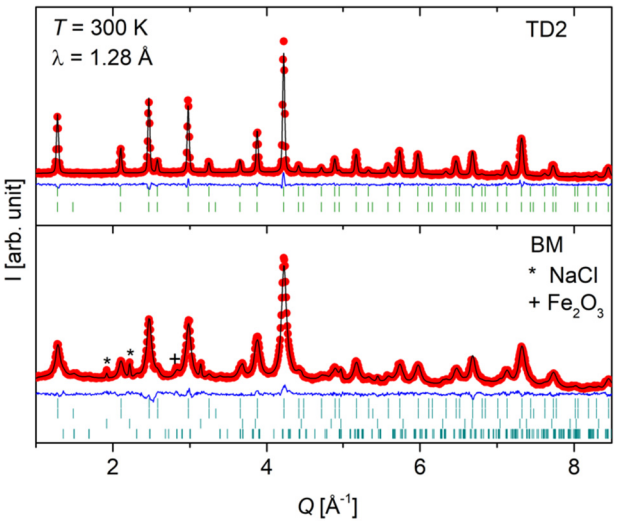

FIG. 2. Neutron powder diffraction data collected at D1B (results shown only for λ = 1.28 Å) and their respective Rietveld refinements. (a) Thermal decomposition sample, TD2. (b) Ball milling sample, BM. Vertical bars indicate Bragg reflections from the cubic Fd3-m space group and magnetic reflections corresponding to a propagation vector $\boldsymbol{k} = (0,0,0)$. (*) and (+) indicate NaCl and Fe_2O_3 impurities, remnant from the synthesis process, which are present in the BM sample and were included in the refinement.

measured temperature (2 K) for sample TD1 are presented in Table II. The obtained net magnetic moment (μ_{ob}) of 3.3 μ_B/f.u. is higher than the value of 2.5 μ_B/f.u. obtained by leaving octahedral moments opposite to the tetrahedral ones, but not constraining their modules to be equal.

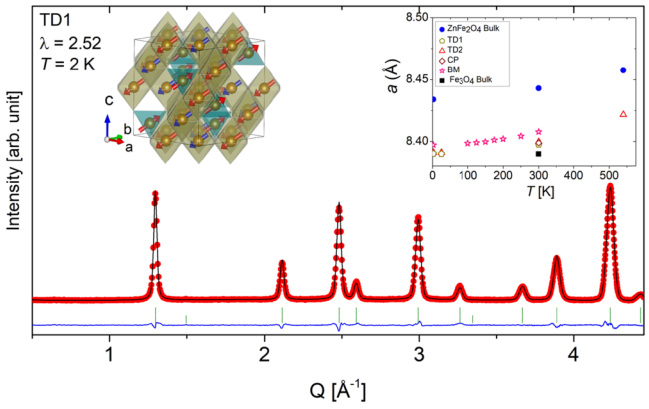

FIG. 3. Rietveld refinement of NPD data at $T = 2$ K collected at D1B using λ = 2.52 Å for the TD1 sample. The left inset illustrates the ferrimagnetic model used in the refinement. Right inset: lattice parameter thermal evolution for all the samples measured with NPD. The pure Zn ferrite $ZnFe_2O_4$, (bulk) is also included using a blue circle. Fe_3O_4 room temperature parameter is included using a black square (45).

Figure 3 presents the Rietveld refinement of NPD data for the TD1 sample using the collinear ferrimagnetic model as previously described. The right inset of the figure depicts the cubic lattice parameter as a function of temperature, which presents a smooth and monotonous behavior across all samples.

In order to explore possible magnetic transitions, data were collected at different temperatures for BM, TD1, and TD2. The thermal evolution of the data does not show signatures of any additional magnetic order beyond what was observed at room temperature.

Macroscopic magnetization measurements

dc magnetization measurements as a function of the applied field were performed to determine the magnetic saturation at 5 K, as presented in Table I. The Ms value determined for TD1 aligns with that of bulk magnetite Fe_3O_4 (98 emu/g), while TD2 exhibits a slightly lower saturation value, approximately 97% of the magnetite value. In contrast, the magnetic saturation for sample CP corresponds to around 87% of that of magnetite, and following the ball milling process, it decreases to 65% of the magnetite saturation observed in bulk magnetite.

The thermal evolution of dc magnetization was measured with an applied field of 100 Oe, employing zero field cooling (ZFC) and field cooling (FC) protocols. The results are presented in Fig. 4. For the BM and CP samples, and the ZFC and FC curves overlap around room temperature, indicating that these samples are in the superparamagnetic regime. As the temperature diminishes below ~250 K, the ZFC and FC curves split, indicating that these MNP samples are partially blocked, in agreement with their effective magnetic anisotropy distribution. On the other hand, samples TD1 and TD2 show an irreversible behavior that persists above room temperature, suggesting that there is a fraction of the particles in a blocked state in the studied temperature range. At low temperatures, the FC curves for the TD systems show an almost flat trend, which could signal magnetic interaction effects. Given that a low concentration of NPs was dispersed in a nonmagnetic epoxy resin, this behavior can be associated with magnetic interactions within the NPs. The strong reduction observed in the ZFC curves may be assigned to a spin-glass freezing process. However, a significant contribution of this process is expected for particles with a diameter blow 15 nm.[46] Thus, some other phenomena should be considered. One possibility is that the relatively broad size distribution of the particles in this sample may result in a small blocking temperature (T_B) for the smaller particles. Following this line, the statistical distribution of the blocking temperature was calculated considering an assembly of non-interacting particles, using (see the supplementary material of Ref. 15)

$$f(T_B) = \frac{1}{T}\frac{d(M_{ZFC} - M_{FC})}{dT}, \quad (1)$$

where M_{ZFC} and M_{FC} are the magnetization values corresponding to the ZFC and FC measurements, respectively. The inset of each panel in Fig. 4 depicts the calculated $f(T_B)$. It is observed that sample TD2 presents a monodispersed distribution with a mean value $\langle T_B \rangle = 29$K, in contrast with sample TD1, which shows three local maxima in the $f(T_B)$ function located at 11, 36, and 86 K. For sample

TABLE II. Structural and magnetic parameters for the TD1 sample obtained from NPD multipattern Rietveld refinement at $T = 2$ K (λ_1 and λ_2). Atomic positions (x, y, z) are described at Fd-3m (origin choice 2) crystallographic group. Magnetic moments are oriented in the ⟨111⟩ direction. Biso correspond to isotropic temperature factors.

	Wycoff position	x	y	z	Biso	Occ
Fe1T	8*a*	0.125	0.125	0.125	0.38 (3)	0.041 54
ZnT	8*a*	0.125	0.125	0.125	0.38 (3)	0.000 13
Fe2o	16*d*	0.5	0.5	0.5	0.47 (3)	0.083 33
O	32*e*	0.2548 (1)	0.2548 (1)	0.2548 (1)	0.14 (3)	0.166 67
a (Å)			8.3916 (1)			
*R*B			1.3			
*r*_mag			4.5			
μ_T (μ_B)			3.87 (1)			
μ_{oa} (μ_B)			3.87 (1)			
μ_{ob} (μ_B)			3.35 (1)			

CP, a low peak is observed in the blocking temperature distribution, around 8 K, but with a relatively higher irreversibility temperature, about 270 K, still much smaller than that observed for samples TD1 and TD2. This behavior can be attributed to several factors: first, the size distribution observed in the TEM analysis, which is much smaller than that observed for samples TD1 and TD2 in both mean diameter and size dispersion, resulting in a much lower blocking temperature and not so high irreversibility temperature; second, a lower effective anisotropy due to the composition richer in Zn or to a larger variation in the cationic environment due to a low crystallinity degree; third, this sample probably presents some NP agglomeration degree. For sample BM, no maximum is observed in the blocking temperature distribution despite the ZFC and FC curves presenting typical features of a blocking process, with an irreversibility temperature around 270 K, which is similar to that of its parent sample CP. However, the very low main blocking temperature indicates either a reduction in the effective anisotropy due to some crystallographic effect, since the composition is similar to that of sample CP, or a reduction in the "effective" crystallite size. In addition, the decrease observed in the low temperature region of the FC curve indicates an increment in the interaction among the NPs, which is expected after the milling process.

It is important to note that the different shapes of the particles can result in changes of magnetic response, mainly the magnetic saturation and the anisotropy.[47,48] However, it is expected that differences in size and crystallinity degree should have a greater effect on the magnetic properties of the nanoparticles.[49] As the MFH

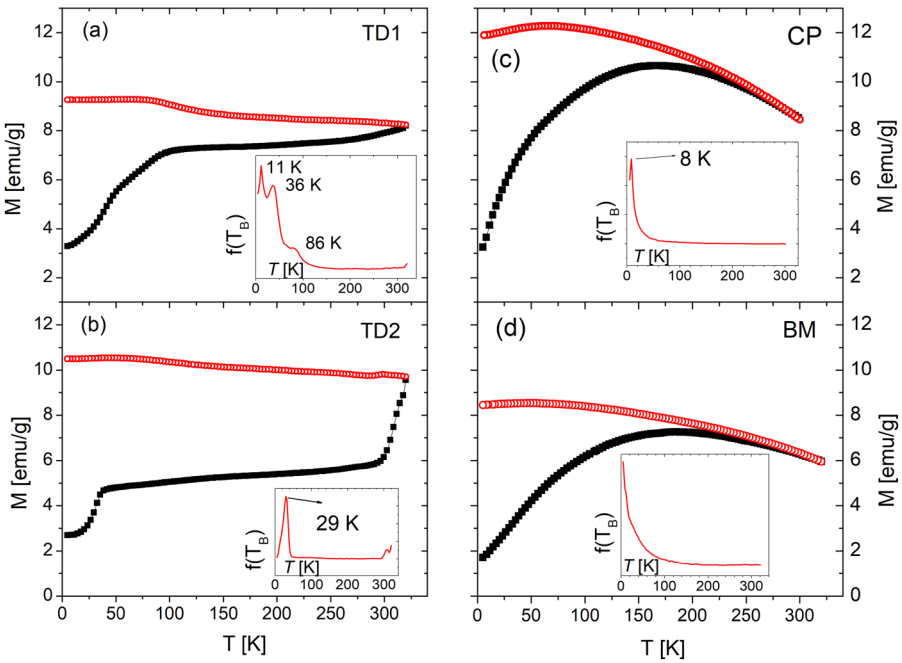

FIG. 4. Temperature dependence of the dc magnetization collected under Zero Field Cooling (solid squares) and Field Cooling (open circles) protocols with an applied field of H = 100 Oe for $Zn_xFe_{3-x}O_4$ nanoparticles synthesized by thermal decomposition (a) and (b), coprecipitation (c), and ball milling (d). The insets show the blocking temperature distribution calculated using Eq. (1).

experiments were performed at room temperature, we also measured the magnetization curves as a function of the applied field at room temperature (see Fig. S4 in the supplementary material). Effectively, we observe a larger reduction of the saturation magnetization at 300 K with respect to the values measured at 5 K for the CP and BM samples, which present lower particle size and crystallinity degree.

Magnetic hyperthermia

Magnetic fluid hyperthermia measurements were carried out on high and low viscosity media in order to investigate the predominant relaxation mechanisms. Figure 5(a) presents magnetic hyperthermia for TD1 and TD2 in a high viscosity medium: oleic acid. It is evident that TD2 exhibits a significantly higher temperature increase compared to TD1. Given that both systems have the same NP concentration, this result indicates that TD2 is more efficient in increasing temperature than TD1. The heating efficiency is quantified by the specific loss power (SLP), which is calculated as

$$\mathrm{SLP} = C_P^{\mathrm{liq}} \left(\frac{m_{\mathrm{liq}}}{m_{\mathrm{NP}}} \right) \frac{dT}{dt}, \tag{2}$$

where C_P is the specific heat capacity of the liquid media, $\left(\frac{m_{\mathrm{liq}}}{m_{\mathrm{NP}}}\right)$ is the mass ratio between liquid and NPs, which is equal to 200 (0.5% wt./wt. NP concentration), and dT/dt was obtained from a linear fit in the range of $40\ \mathrm{s} < t < 60\ \mathrm{s}$. SLP values are displayed in Table I.

Figure 5(b) presents magnetic hyperthermia measurements for TD1 and TD2 in a low viscosity medium, hexane, where it is clear that TD2 does not produce heat (the negative slope corresponds to a loss of heat by the coil's refrigerator water). On the other hand, TD1 exhibits a temperature increase in both media, but the SLP values are $<12\ \mathrm{W}/g_{\mathrm{MNP}}$ in hexane. This indicates that these particles are not optimized for magnetic hyperthermia. Note the difference in the vertical scale with respect to the high viscosity medium results.

Figure 5(c) presents BM and CP magnetic hyperthermia measurements in a high viscosity medium, triethylene glycol, both showing a temperature increment when a magnetic ac field is applied. The results indicate that the temperature increase rates for CP are greater than for BM. Both samples have the same composition but the BM NPs are less crystalline due to the milling process, which aligns with the difference observed between their respective M_S values measured at 5 K.

Figure 5(d) shows the low viscosity magnetic hyperthermia measurement for CM and BM. SLP values are lower than in high viscosity media. Also, in this case, the SLP values for CP are greater than those for BM.

In general, a higher SLP value is associated with a system having a higher degree of crystallinity or a larger M_S. However, the response of nanoparticulated systems involves many other factors. The absorption of field energy by the NPs, for the subsequent conversion into heat, depends on the dephasing of the applied field and the magnetic moment of the particle. In the case of NPs dispersed in a medium with high viscosity, where the Néel relaxation mechanism dominates, the magnetic reversion through an energy barrier plays a crucial role. For a monodomain system, this reversion is primarily influenced by the $K_{\mathrm{eff}}V$ product. However, different relaxation mechanisms are expected to be relevant for systems

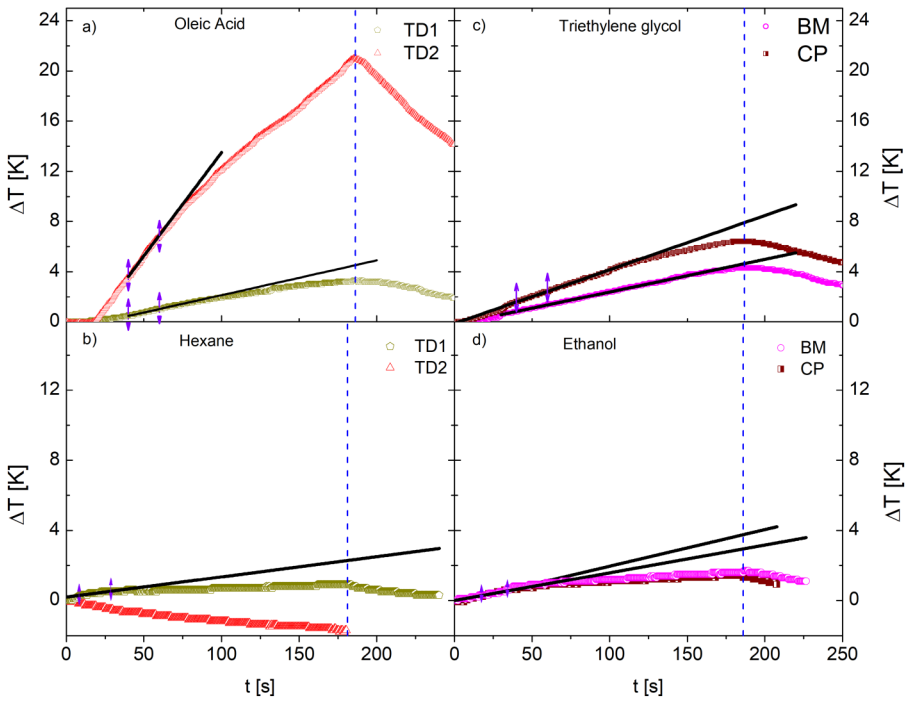

FIG. 5. Temperature increments as a function of time in fluid magnetic hyperthermia measurements in different media. Frequency = 571 kHz, amplitude H_0 = 200 Oe. Vertical dashed lines indicate the time when the magnetic field is turned off. Solid lines indicate linear fits in the $40\ \mathrm{s} < t < 60\ \mathrm{s}$ range for (a) and (c) and between $10\ \mathrm{s} < t < 30\ \mathrm{s}$ for (b) and (d).

with low crystallinity, those where the presence of a diamagnetic ion reduces the super-exchange interaction within the crystal structure or for those with high crystallinity with a size close to the upper monodomain limit. Additionally, the initial susceptibility, which generally depends on the power of the applied field and the square of the effective moment of the particle, is another crucial factor. Once again, this initial susceptibility is influenced by parameters related to the composition, morphology, and crystallinity of the nanoparticles. Finally, in the case of ferrites, particularly Zn ferrites, there is a strong dependence on the inversion degree. Considering the differences in size and in composition, crystallinity, or morphology in the set of samples studied in this work, these factors contribute to a distinctly varied magnetic response and different performances in MFH experiments under the same applied field.

Sample TD2 demonstrates superior performance in terms of temperature increment. Both TD1 and TD2 exhibit MFH performance under different solvents, indicating the predominance of Néel relaxation for high viscosity, with characteristics resulting in a relatively good response in such condition. In contrast, a strong predominance of the Brown mechanism is evident for the solvent with lower viscosity, leading to a suboptimal response in MFH experiments. Considering the particle size, no heating efficiency was expected for either mechanisms, since for Zn ferrite NPs with a similar composition, the optimum size for a strong MFH performance is much lower, around 15–25 nm.[15] This may indicate that probably, the reduction in the anisotropy due to the presence of the Zn and the relatively large particle size result in a magnetic relaxation mechanism that cannot be so easily described as the one for a monodomain system. In the case of more complex magnetic relaxation mechanisms, the compositional, morphological, and crystallographic (including the inversion degree) properties of the NPs, and the resulting magnetic properties, play different roles than those expected for a monodomain system. Therefore, a comprehensive characterization of the system becomes crucial for understanding and optimizing the response in MHF experiments.

For samples CP and BM, the comparison can be drawn in different terms. Although both exhibit a similar morphology and composition, their crystallographic properties differ. The reduction in the M_S and anisotropy promoted by the lower crystallinity degree of the BM sample results in poor performance in MFH experiments in a medium with high viscosity, where the Néel mechanism dominates, when compared to its parent sample CP. In these two samples, the lower crystallinity degree due to the synthesis method and the resulting magnetic properties again emerge as determining factors for the response in the MFH experiments. Thus, a deep characterization of the system remains crucial for understanding and optimizing such responses.

SUMMARY

Zn-ferrite NPs were synthesized and characterized through various methods. PIXE results revealed Zn/Fe ratios lower than the nominal values in samples prepared by thermal decomposition, whereas the coprecipitation route achieved nominal Zn concentration, allowing for a higher Zn content in ferrite samples. Neutron diffraction data analysis indicated that in ball milling and thermal decomposition methods, Zn atoms are sitting exclusively at the tetrahedral site of the spinel structure. Magnetic hyperthermia measurements in fluid demonstrated that the presence of Zn induces changes in the magnetic anisotropy. Specifically, the sample with $x = 0.09$ fabricated by thermal decomposition (TD2) exhibited the highest SLP value in a high viscosity medium, suggesting an enhancement in relaxation due to Zn addition. In essence, the magnetic properties of sample TD2, primarily influenced by its composition, result in superior hyperthermia performance compared to its counterpart TD1. Despite a decrease in magnetic saturation of the ferrite caused by the addition of Zn at a tetrahedral site, an improvement in SLP value was observed. Our findings suggest that the improvement in MHF properties is associated with a change in anisotropy induced by Zn addition rather than with Zn occupying an octahedral site.

SUPPLEMENTARY MATERIAL

See the supplementary material for additional figures omitted from the main manuscript for brevity. Figure S1 displays a TEM image of the TD2 sample, where nanoparticles formed by two crystals are shown. In Fig. S2, we present thermodiffraction data for TD2 collected at $\lambda = 2.52$ Å^{-1}. Figure S3 exhibits the magnetization vs magnetic field at $T = 5$ K for the different $Zn_xFe_{3-x}O_4$ nanoparticles that were employed to extract the saturation magnetization values informed in Table I. Figure S4 shows the M vs H curves measured at room temperature for the four studied samples.

ACKNOWLEDGMENTS

We acknowledge financial support of the European Commission through Marie Skłodowska-Curie Actions H2020 RISE with the projects NESTOR (Grant No. 101007629), SPICOLOST (Grant No. 734187), and ULTIMATE-I (Grant No. 101007825). Also, J.L. and D.T. acknowledge support of ANPCyT though Project No. PICT-2019-01849.

AUTHOR DECLARATIONS

Conflict of Interest

The authors have no conflicts to disclose.

Author Contributions

J. Lohr: Conceptualization (equal); Formal analysis (equal); Investigation (equal); Visualization (equal); Writing – original draft (equal). **D. Tobia:** Conceptualization (equal); Formal analysis (equal); Investigation (equal); Visualization (equal); Writing – original draft (equal). **T. E. Torres:** Formal analysis (equal); Investigation (equal); Visualization (equal); Writing – review & editing (equal). **L. Rodríguez:** Formal analysis (equal); Investigation (equal); Writing – review & editing (equal). **I. Puente Orench:** Data curation (equal); Formal analysis (equal); Investigation (equal); Writing – review & editing (equal). **G. J. Cuello:** Data curation (equal); Formal analysis (equal); Investigation (equal); Writing – review & editing (equal). **M. H. Aguirre:** Funding acquisition (equal); Writing – review & editing (equal). **J. Campo:** Funding acquisition (equal); Writing – review

& editing (equal). **G. Aurelio:** Conceptualization (equal); Formal analysis (equal); Investigation (equal); Project administration (equal); Writing – original draft (equal). **E. Lima:** Conceptualization (equal); Formal analysis (equal); Funding acquisition (equal); Investigation (equal); Project administration (equal); Writing – original draft (equal).

DATA AVAILABILITY

The data that support the finding of this study are available from the corresponding author upon reasonable request.

REFERENCES

[1]D. Ling, N. Lee, and T. Hyeon, "Chemical synthesis and assembly of uniformly sized iron oxide nanoparticles for medical applications," Acc. Chem. Res. **48**, 1276–1285 (2015).

[2]N. Abid, A. M. Khan, S. Shujait, K. Chaudhary, M. Ikram, M. Imran, J. Haider, M. Khan, Q. Khan, and M. Maqbool, "Synthesis of nanomaterials using various top-down and bottom-up approaches, influencing factors, advantages, and disadvantages: A review," Adv. Colloid Interface Sci. **300**, 102597 (2022).

[3]D. Stanicki, L. V. Elst, R. N. Muller, and S. Laurent, "Synthesis and processing of magnetic nanoparticles," Curr. Opin. Chem. Eng. **8**, 7–14 (2015).

[4]H. L. Andersen, M. Saura-Múzquiz, C. Granados-Miralles, E. Canévet, N. Locke, and M. Christensen, "Crystalline and magnetic structure-property relationship in spinel ferrite nanoparticles," Nanoscale **10**, 14902–14914 (2018).

[5]B. Pacakova, S. Kubickova, G. Salas, A. R. Mantlikova, M. Marciello, M. P. Morales, D. Niznansky, and J. Vejpravova, "The internal structure of magnetic nanoparticles determines the magnetic response," Nanoscale **9**, 5129–5140 (2017).

[6]T. Tajiri, H. Deguchi, M. Mito, K. Konishi, S. Miyahara, and A. Kohno, "Effect of size on the magnetic properties and crystal structure of magnetically frustrated $DyMn_2O_5$ nanoparticles," Phys. Rev. B **98**, 064409 (2018).

[7]T. Tajiri, K. Sakai, H. Deguchi, M. Mito, and A. Kohno, "Size effects on magnetic property and crystal structure of Mn_3O_4 nanoparticles in mesoporous silica," IEEE Trans. Magn. **55**, 2300204 (2019).

[8]R. E. Rosensweig, "Heating magnetic fluid with alternating magnetic field," J.: Magn. Magn. Mater. **252**, 370–374 (2002).

[9]N. A. Usov and B. Ya. Liubimov, "Dynamics of magnetic nanoparticle in a viscous liquid: Application to magnetic nanoparticle hyperthermia," J. Appl. Phys. **112**, 023901 (2012).

[10]Q. Qin, Y. Zhou, P. Li, Y. Liu, R. Deng, R. Tang, N. Wu, L. Wan, M. Ye, H. Zhou, and Z. Wang, "Phase-transition nanodroplets with immunomodulatory capabilities for potentiating mild magnetic hyperthermia to inhibit tumour proliferation and metastasis," J. Nanobiotechnol. **21**, 131 (2023).

[11]A. Gallo-Cordova, J. J. Castro, E. L. Winkler, E. Lima Jr, R. D. Zysler, M. P. Morales, J. G. Ovejero, and D. A. Streitwieser, "Improving degradation of real wastewaters with self-heating magnetic nanocatalysts," J.: Clean. Prod. **308**, 127385 (2021).

[12]S. Ganguly and S. Margel, "Design of magnetic hydrogels for hyperthermia and drug delivery," Polymers **13**, 4259 (2021).

[13]I. Sharifi, H. Shokrollahin, and S. Amiri, "Ferrite-based magnetic nanofluids used in hyperthermia applications," J. Magn. Magn. Mater. **324**, 903–915 (2012).

[14]R. Kappiyoor, M. Liangruksa, R. Ganguly, and I. K. Puri, "The effects of magnetic nanoparticle properties on magnetic fluid hyperthermia," J. Appl. Phys. **108**, 094702 (2010).

[15]A. A. Almeida, E. De Biasi, M. Vasquez Mansilla, D. P. Valdés, H. E. Troiani, G. Urretavizcaya, T. E. Torres, L. M. Rodríguez, D. E. Fregenal, G. C. Bernardi, E. L. Winkler, G. F. Goya, R. D. Zysler, and E. Lima, Jr., "Magnetic hyperthermia experiments with magnetic nanoparticles in clarified butter oil and paraffin: A thermodynamic analysis," J. Phys. Chem. C **124**, 27709 (2020).

[16]J. Smit and H. P. J. Wijn, *Ferrites—Physical Properties and Technical Applications* (Philips' Technical Library, NATLAB, Eindhoven, 1959).

[17]G. C. Lavorato, M. E. Saleta, S. J. A. Figueroa, D. Tobia, J. C. Mauricio, J. Lohr, E. Baggio-Saitovitch, H. E. Troiani, R. D. Zysler, E. Lima, and E. L. Winkler, "Cation occupancy in bimagnetic CoO-core/$Co_{1-x}Zn_xFe_2O_4$-shell (x = 0–1) nanoparticles," J. Alloy. Compd. **877**, 160172 (2021).

[18]S. J. Stewart, S. J. A. Figueroa, J. M. Ramallo López, S. G. Marchetti, J. F. Bengoa, R. J. Prado, and F. G. Requejo, "Cationic exchange in nanosized $ZnFe_2O_4$ spinel revealed by experimental and simulated near-edge absorption structure," Phys. Rev. B **75**, 073408 (2007).

[19]M. A. Cobos, P. de la Presa, I. Llorente, J. M. Alonso, A. García-Escorial, P. Marín, A. Hernando, and J. A. Jimenez, "Magnetic phase diagram of nanostructured zinc ferrite as a function of inversion degree δ," J. Phys. Chem. C **123**, 17472 (2019).

[20]P. Wright, A. M. Bell, and J. P. Attfield, "Variable temperature powder neutron diffraction study of the verwey transition in magnetite Fe_3O_4," Solid State Sci. **2**, 747 (2000).

[21]P. Whitfield, "Quantitative phase analysis of challenging samples using neutron powder diffraction. Sample #4 from the CPD QPA round robin revisited," Powder Diffr. **31**(3), 192 (2016).

[22]J. M. Hastings and L. M. Corliss, "An antiferromagnetic transition in zinc ferrite,' Phys. Rev. **102**, 1460 (1956).

[23]U. Konig, E. F. Bertaut, Y. Gros, M. Mitrikov, and G. Chol, "Models of the magnetic structure of zinc ferrite," Solid State Commun. **8**, 759 (1970).

[24]T. Sato, K. Haneda, M. Seki, and T. Iijima, "Morphology and magnetic properties of ultrafine ZnFe2O4 particles," Appl. Phys. A **50**, 13 (1990).

[25]F. S. Li, L. Wang, J. B. Wang, Q. G. Zhou, X. Z. Zhou, H. P. Kunkel, and G. Williams, "Site preference of Fe in nanoparticles of $ZnFe_2O_4$," J. Magn. Magn. Mater. **268**, 332 (2004).

[26]M. Hofmann, S. J. Campbell, H. Ehrhardt, and R. Feyerherm, "The magnetic behaviour of nanostructured zinc ferrite," J. Mater. Sci. **39**, 5057 (2004).

[27]H. Ehrhardt, S. J. Campbell, and M. Hofmann, "Magnetism of the nanostructured spinel zinc ferrite," Scr. Mater. **48**, 1141 (2003).

[28]S. D. Kaushik, "Neutron as a tool to study the structural and other properties of magnetic nanoparticles," in *Fundamentals and Industrial Applications of Magnetic Nanoparticles Woodhead Publishing Series in Electronic and Optical Materials*, edited by C. M. Hussain and K. K. Patankar (Woodhead Publishing, Sawston-Cambridge, 2022), pp. 153–164.

[29]J. M. DeTeresa, M. D. Mukadam, J. Kohlbrecher, M. R. Ibarra, J. Arbiol, P. Sharma, and S. K. Kulshreshtha, "Experimental study of the structural and magnetic properties of γ-Fe_2O_3 nanoparticles," Phys. Rev. B **74**, 224428 (2006).

[30]V. Blanco-Gutierrez, E. Climent-Pascual, M. J. Torralvo-Fernandez, R. Saez-Puche, and M. T. Fernandez-Diaz, "Neutron diffraction study and superparamagnetic behavior of $ZnFe_2O_4$ nanoparticles obtained with different conditions," J.: Solid State Chem. **184**, 1608 (2011).

[31]S. Limandri, C. Olivares, L. Rodriguez, G. Bernardi, and S. Suárez, "PIXE facility at Centro Atómico bariloche," Nucl. Instrum. Methods Phys. Res. Sect. B **318**, 47 (2014).

[32]J. L. Campbell, N. I. Boyd, N. Grassi, P. Bonnick, and J. A. Maxwell, "The Guelph PIXE software package IV," Nucl. Instrum. Methods Phys. Res. Sect. B **268**(20), 3356 (2010).

[33]J. H. Lohr, M. H. Aguirre, J. Campo, C. V. Colin, G. J. Cuello, G. Goya, E. Lima Jr., V. Nassif, M. Pardo-Sainz, and I. Puente Orench, "Zn distribution and magnetic order in $Zn_xFe_{3-x}O_4$ ferrite nanoparticles for biomedical applications as a function of Zn content," Institut. Laue-Langevin (ILL) (2020).

[34]J. Rodríguez-Carvajal, Abstracts of the Satellite Meeting on Powder Diffraction of the XV Congress of the IUCr, Toulouse (1990), p. 127.

[35]J. Rodríguez-Carvajal, "Recent advances in magnetic structure determination by neutron powder diffraction," Phys. B **192**(1–2), 55 (1993).

[36]E. Solano, C. Frontera, T. Puig, X. Obradors, S. Ricart, and J. Ros, "Neutron and x-ray diffraction study of ferrite nanocrystals obtained by microwave-assisted growth. A structural comparison with the thermal synthetic route," J. Appl. Cryst. **47**(1), 414 (2014).

[37]D. Sagdeev, I. Gabitov, C. Isyanov, V. Khairutdinov, M. Farakhov, Z. Zaripov, and I. Abdulagatov, "Densities and viscosities of oleic acid at atmospheric pressure," J. Am. Oil Chem. Soc. **96**, 647 (2019).
[38]S. I. Mekhtiev, A. A. Mamedov, S. K. Khalilov, and M. A. Aleskerov, "Experimentelle Untersuchung des Einflusses von Octylmethacrylat auf Viskosität und Dicht der Kohlenwasserstoffe," Izv. Vyssh. Uchebn. Zaved., Neft Gaz **3**, 64–100 (1975).
[39]D. I. Sagdeev, M. G. Fomina, G. K. Mukhamedzyanov, and I. M. Abdulagatov, "Experimental study of the density and viscosity of polyethylene glycols and their mixtures at temperatures from 293 K to 465 K and at high pressures up to 245 MPa," Fluid Phase Equilib. **315**, 64 (2012).
[40]M. García-Mardones, I. Gascón, M. Carmen López, F. M. Royo, and C. Lafuente, "Viscosimetric study of binary mixtures containing pyridinium-based ionic liquids and alkanols," J. Chem. Eng. Data **57**(12), 3549–3556 (2012).
[41]J. Lohr, A. A. de Almeida, M. S. Moreno, H. Troiani, G. F. Goya, T. E. Torres Molina, R. Fernandez-Pacheco, E. L. Winkler, M. Vásquez Mansilla, R. Cohen, L. C. C. M. Nagamine, L. M. Rodríguez, D. E. Fregenal, R. D. Zysler, and E. Lima Jr., "Effects of Zn substitution in the magnetic and morphological properties of Fe-oxide-based core–shell nanoparticles produced in a single chemical synthesis," J. Phys. Chem. C **123**(2), 1444–1453 (2019).
[42]S. A. Degterov, A. D. Pelton, and E. Jak, "Experimental study of phase equilibria and thermodynamic optimization of the Fe-Zn-O system," Metall. Mater. Trans. B **32**, 643 (2001).
[43]M. A. Cobos, P. de la Presa, I. Puente-Orench, I. Llorente, I. Morales, A. García-Escorial, A. Hernando, and J. A. Jiménez, "Coexistence of antiferro- and ferrimagnetism in the spinel $ZnFe_2O_4$ with an inversion degree δ lower than 0.3," Ceram. Int. **48**, 12048 (2022).
[44]S. Nakashima, K. Fujita, K. Tanaka, K. Hirao, T. Yamamoto, and I. Tanaka, "First-principles XANES simulations of spinel zinc ferrite with a disordered cation distribution," Phys. Rev. B **75**, 174443 (2007).
[45]B. D. Cullity and C. D. Graham, *Introduction to Magnetic Materials* (John Wiley & Sons, Pag, 2011), pp. 178–183.
[46]E. Lima, Jr., E. De Biasi, M. Vasquez Mansilla, M. E. Saleta, F. Effenberg, L. M. Rossi, R. Cohen, H. R. Rechenberg, and R. D. Zysler, "Surface effects in the magnetic properties of crystalline 3 nm ferrite nanoparticles chemically synthesized," J. Appl. Phys. **108**, 103919 (2010).
[47]H. Gavilán, K. Simeonidis, E. Myrovali, E. Mazarío, O. Chubykalo-Fesenko, R. Chantrell, L. Balcells, M. Angelakeris, M. P. Morales, and D. Serantes, "How size, shape and assembly of magnetic nanoparticles give rise to different hyperthermia scenarios," Nanoscale **13**, 15631 (2021).
[48]A. G. Kolhatkar, A. C. Jamison, D. Litvinov, R. C. Willson, and T. Randall Lee, "Tuning the magnetic properties of nanoparticles," Int. J. Mol. Sci. **14**, 15977–16009 (2013).
[49]N. M. Deraz, "Size and crystallinity-dependent magnetic properties of copper ferrite nanoparticles," J. Alloy Compd. **501**, 317–325 (2010).